

SIMULATION AND MEASUREMENT OF THERMAL FLUXES IN LOAD-BEARING BONDED FRP SINGLE-LAP JOINTS

14th ECSSMET, 27-30 September 2016, Toulouse, France

Michael Lange⁽¹⁾, Volodymyr Baturkin⁽²⁾, Christian Hühne⁽¹⁾, Olaf Mierheim⁽¹⁾

⁽¹⁾ DLR – German Aerospace Center, Lilienthalplatz 7, 38100 Braunschweig,
Tel.: +49 531 295-3223, Email: M.Lange@dlr.de

⁽²⁾ DLR – German Aerospace Center, Robert-Hooke-Straße 7, 28359 Bremen,
Tel.: +49 421 24420-1610, Email: Volodymyr.Baturkin@dlr.de

ABSTRACT

Fibre reinforced plastics are a commonly used material for primary and secondary spacecraft structures. Besides their excellent mechanical properties, they offer a high potential for thermal applications. At the moment this combined potential of thermal and mechanical material properties is usually limited to the design and simulation of secondary composite's structures. If both potentials would be combined on full spacecraft level, too, further mass and savings are possible. Hence, it is sought to connect the thermal and structural design in a combined semi-analytical mechanical and thermal 2D/3D FE simulation technique. As a prerequisite this paper focuses on the investigation of an exemplarily load-bearing bonded single-lap joint coupon of two CFRP laminates. The temperature distribution in the coupon is calculated analytically, numerically and subsequently measured in a corresponding thermal vacuum test. It is discussed what are the differences in the analytical and numerical solution and what is required before correlating the results.

1. INTRODUCTION

Fibre reinforced plastics (FRP), especially Carbon-FRPs (CFRP), are a commonly used material for primary and secondary spacecraft structures. To achieve optimal results, the (composite) structures' design process needs to consider the distinctive orthotropic mechanical properties. Available for this purpose, are corresponding finite element (FE) simulation techniques and analysis criteria. They enable the engineer to investigate composite structures from the component level up to the full spacecraft level and to achieve the most appropriate design for the materials involved.

Besides their excellent mechanical properties, FRPs also offer a high potential for thermal applications. Pitch fibre reinforcements, for example, can have thermal conductivities (TC) of 620 W/mK [1] in fibre direction or more. At the moment this combined potential of mechanical and thermal material properties is usually limited to the design and simulation of secondary composite's structures. A few examples of secondary structures are presented by Klebor et al. [2], Ihle et al. [3] or Katajisto et al. [4].

As noted by Kulkarni and Brady [5], what is missing is a systematic and comprehensive approach, which allows designing FRP structures with specific directional thermal conductivities or to run 'what if' type simulations to assess variations in the laminate build-up on the global conductivities. Hence, they do not take into account the influences of the microstructure on the macrostructure, but rather start at the influence on conductivity by changes on the ply level.

In order to allow the simulation of such a comprehensive approach for hybrid structures, especially spacecraft thermal protection systems, Noack [6] developed two corresponding finite elements (QUADLLT and QUADQLT). These 2D layered elements allow not only the stress and strain (thermo-mechanical) calculation, but also a simultaneous calculation of thermal gradients (linear and quadratic respectively) in the element's normal and in-plane directions. Further, Noack discusses the 2D-2D coupling of the developed elements in order to simulate structures with

varying layups and/or thicknesses. Additionally a 2D-3D (see Fig. 1) coupling is presented for cases where a concentrated heat load is introduced in a region of 3D elements. For model size reduction these are connected to 2D elements that simulate the remaining structure aside the areas of applied heat loads. The drawback, as with many other approaches, is that the QUADLLT and QUADQLT elements are not available in any commercial finite element program.

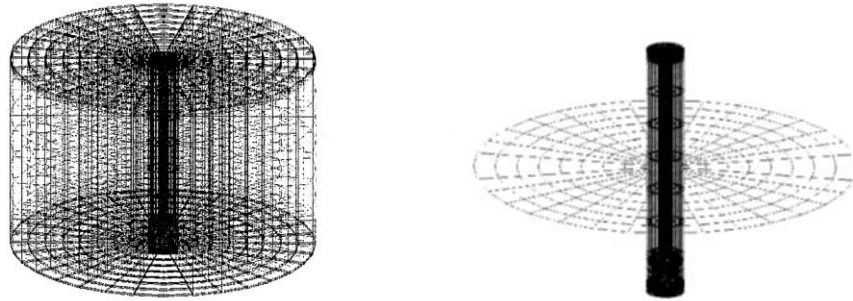


Fig. 1. Insert with surrounding structure. Complete 3D meshing (left). 3D meshing for the insert and 2D meshing for the surrounding structure (right). [6]

Noack's technique used up by Rolfes et al. [7] and suggested for an application in the thermal/thermo-mechanical concurrent engineering of composite airframe structures. What is in these cases required are tools that allow a quick trade-off between different design concepts but at the same time deliver an accurate enough simulation of the resulting pre-design.

This becomes even more obvious when structures are small and serve itself as a conductive interface, as described by Celotti [8] on the example of the MASCOT structure(s). Celotti states that "the whole system is interconnected creating a unique environment and each interface cannot be studied and evaluated without considering the influence of all the others." Consequently a sophisticated thermal design strategy is needed to keep each component within its temperature limits. This includes especially the thermal interfaces and their modelling, which requires after each thermal vacuum test a correlation of the thermal model with the test results. While the typical maximal deviation between a correlated thermal model and measurements for relevant components is tuned to 5 – 11 °C [8, 9], in MASCOT only 3 °C variation are allowed.

Hence, the approach of a simultaneous thermal and structural design process in an early design phase is especially for composite structures advantageous, as the conductivities, the strength and the stiffness change at the same time significantly with the layup. If both potentials are combined on full spacecraft level, further mass savings are believed to be possible. In addition the development time and costs should reduce, while the design's reliability increases.

Therefore some basic investigations for a FE simulation technique with a combined full structural and reduced (or preliminary) thermal analysis capability in Patran/Nastran shall be introduced. In difference to an actual simultaneous or concurrent engineering process a solely iterative scheme is sought. This is based on a method that incorporates the Patran/Nastran FE program creating in a first step a 2D element model for classical structural analysis. When a structural pre-design is found, the model can be expanded for an additional reduced thermal analysis capability by means of a semi-analytical approach and corresponding FE modelling. This allows an immediate feedback to the thermal engineer about the prospective effective thermal conductivity of the current structural design and tentative design adaptations, if required.

As mentioned by Celotti, the key aspects of the reduced thermal analysis in composite structures are the regions with relevant out-of-plane heat fluxes, id est joints and interfaces. What is often unknown, are especially the out-of-plane thermal conductivities and heat fluxes, respectively. Neither can they be properly simulated in structural models consisting of 1D and 2D elements only [10]. Although an initially complete 3D formulation would overcome the modelling issue, a combined 2D/3D or 2.5D solution must be preferred for design studies in terms of calculation time and flexible design changes. Patran provides the 3D PCOMPLS elements that can be created via a

(local) conversion of 2D shell elements (e.g. PCOMPG). The converted elements allow the simulation of temperature gradients in the element's in-plane and also element-normal direction. However, the PCOMPLS elements work basically well for plane or continuously curved structures, but not in (perpendicular) jointed parts. The example in Fig. 2 shows for a T-joint that the 3D PCOMPLS elements (grey) connect only at the section (green) of the underlying 2D shell elements (red). The other PCOMPLS elements, such as highlighted exemplarily with blue circles, do not connect. Consequently, any interaction between them is prevented.

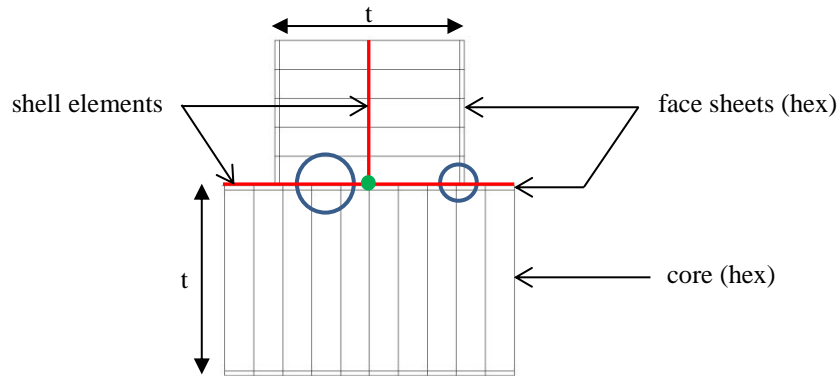


Fig. 2. From 2D shell elements extruded PCOMPLS hex elements at a T-joint.

To fill this gap, the actual thermal and structural properties describing the joints or interfaces are first to be determined in coupon level tests and then ‘design-dependent translated’ in a 2.5D FE model. The present paper focuses on the coupon level tests. Exemplarily a generic single-lap joint (SLJ) of two CFRP laminates is analysed and simulated with 3D FEs. After the numerical simulation follows an analytical (temperature) calculation and the presentation of the results stemming from a corresponding thermal vacuum test. Finally, the numerical and analytical results are compared to each other and to the measurements before the paper concludes with an outlook to the next steps.

2. NUMERICAL ANALYSIS

The applied test method for the thermal conductivity measurements on the SLJ is based on the Searle’s bar system (cf. [11]). Similarly Baturkin [12] measured the thermal conductivity of CFRP bars with a test setup comparable to that delineated in Fig. 7. It is the basis for the measurements conducted afterwards and will be introduced further in paragraph 5. The main difference in the present paper is the added SLJ, whose influence on the effective conductivity is investigated. Therefore the ‘bar’ is split up into two thin laminates with 2 – 4 plies each. The laminates are jointed in the middle and glued into flanges at the other ends (see Fig. 3 and Fig. 4).

Prior to the thermal test row, a numerical analysis and a parameter study are conducted, which have the following 3 objectives:

1. Investigate the required area or flange size in order to establish a quasi-1-D temperature profile in the thickness direction of the test specimen at $x=0$ mm.
2. Estimate the required power level in order to induce a temperature difference between the temperature sensors (TS) TS-1 and TS-4 (see Fig. 4) of 8-10 K. This allows on the one hand a better resolution and differentiation of influences due to changes in the laminates and a limitation of radiation effect. On the other hand the effect on the conductivities temperature dependency is minimized.
3. Anticipate the test results that will be obtained with the thermal test row.

In order to perform the analyses the **FE-Model** incorporates several parameters (see **Material Properties** and Tab. 1) identified a priori as being influential on the resulting temperature distribution and the load bearing capacity of the joint.

The selected model and specimen dimensions are based on an interface design as applied for the MASCOT Landing Module and its Mechanical & Electrical Interface Support System [13]. There, separate sandwich walls or solid CFRP struts are interconnected with shear patches. However these SLJs can be thought for other (spacecraft) structures, too.

Test Cases

The following Tab. 1 lists the design parameters for the three SLJ specimen investigated in the present paper. Test case #1 is the reference specimen, while for case #2 the jointed length is extended and for case #3 the jointed width. The other parameters remain unchanged.

Tab. 1. Specimen design definition.

Test Case	Specimen design		Test case description
	Laminate-1	Laminate-2	
#1			<p><i>Reference Specimen</i></p> <p>W_1 = 20 mm L_j-1 = 10 mm (=l_{ij} in eq. 8 and 9) L_1 = 70 mm L_{fl} = 15 mm t_{lam1} (n_{lam1}) = 0.25 mm (2) t_{lam2} (n_{lam2}) = 0.5 mm (2) t_{glue} = 0.15 mm</p>
#2			<p><i>Extension of overlapping length</i></p> <p>W_1 = 20 mm L_j-2 = 20 mm (=l_{ij} in eq. 8 and 9) L_2 = 75 mm L_{fl} = 15 mm t_{lam1} (n_{lam1}) = 0.25 mm (2) t_{lam2} (n_{lam2}) = 0.5 mm (2) t_{glue} = 0.15 mm</p>
#3			<p><i>Extension of overlapping width</i></p> <p>W_2 = 30 mm L_j-1 = 10 mm (=l_{ij} in eq. 8 and 9) L_1 = 70 mm L_{fl} = 15 mm t_{lam1} (n_{lam1}) = 0.25 mm (2) t_{lam2} (n_{lam2}) = 0.5 mm (2) t_{glue} = 0.15 mm</p>

Material Properties

The thermal conductivity of a general FRP laminate is defined by the a priori known conductivities of the individual plies [5, 14]. These are the longitudinal conductivity κ_A in fibre direction and the transversal (in- and out-of-plane) conductivity κ_T normal to the fibre direction. While κ_A is calculated by the rule of mixture [14], every analytical approach to calculate κ_T requires the knowledge of the fibres transversal conductivity κ_T^f . κ_T^f is very difficult to be measured directly and only a very limited number of actual measurement results are published. Therefore in the calculations and experiments presented in this paper a CFRP material (M44J/MTM46) with known transversal conductivity κ_T is used. This allows us to specify the so-called directional or effective thermal conductivity for any laminate, consisting of n individual M44J/MTM46 plies and in

different directions θ with respect to the global axial direction. As a result the monoclinic tensor $\bar{\kappa}$, Eq. 1, can be calculated from κ_A and κ_T [14]:

$$\bar{\kappa} = \begin{bmatrix} \kappa_{11} & \kappa_{12} & 0 \\ \kappa_{21} & \kappa_{22} & 0 \\ 0 & 0 & \kappa_{33} \end{bmatrix} \quad (1)$$

What simplifies $\bar{\kappa}$ further is that for balanced bidirectional laminates the coupling term is $\kappa_{12} = \kappa_{21} = 0$ [14, 15]. This applies for all laminates (laminates-1, laminates-2) to be calculated in the present paper. Their effective conductivities are determined from the laminates' ply layup and the constituent material's properties in Tab. 2, while the isotropic glues' conductivities can be set directly.

Laminates-1 has in every test case an unidirectional layup made up from UD-ply M40J-UD/MTM46, $f_{vol}=54\%$. The two plies, each 0.125 mm in thickness, are orientated in the global x-direction. The laminate's effective conductivity $\kappa_{lam1-11}$ is calculated by the rule of mixture. Assuming the matrix' (epoxy) conductivity to 0.20 W/mK, this results in [14]:

$$\kappa_A = \kappa_{11} = \kappa_{lam1-11} = 0.54 * 68.62 \text{ W/mK} + 0.46 * 0.2 \text{ W/mK} = 37.15 \text{ W/mK} \quad (2)$$

The transversal conductivity is:

$$\kappa_T = \kappa_{22} = \kappa_{33} = \kappa_{lam1-22} = 0.66 \text{ W/mK} \quad (3)$$

and was measured in a separate experiment at DLR by the Transient Hot Bridge method [16].

Also laminates-2 is made up from M40J-UD/MTM46 UD-ply with a fiber volume of $f_{vol}=54\%$. It consists of alternating draped UD-ply ($\pm\theta = \pm 45^\circ$) that has a quasi-isotropic conductivity of

$$\begin{aligned} \kappa_A = \kappa_T = \kappa_{11} = \kappa_{22} = \kappa_{lam2-11} = \kappa_{lam2-22} \\ = \frac{1}{4 * 0.125 \text{ mm}} \left[4 * 0.125 \text{ mm} * \left(0.5 * 68.62 \frac{\text{W}}{\text{mK}} + 0.5 * 0.2 \frac{\text{W}}{\text{mK}} \right) \right] = 34.41 \text{ W/mK} \end{aligned} \quad (4)$$

In contrast to unidirectional laminates-1, for the out-of-plane transversal conductivity of laminates-2 might apply that $\kappa_{33} \neq \kappa_{22}$. But because there is no common result in literature for the dependence of κ_{33} on the laminate's layup, it is assumed to be the same for all fabric and UP-ply stackings.

The SLJ is bonded with Araldite 2014-1 and each of the laminates glued with ECCOBOND 285 to the flanges 1 and 2, respectively. The latter ones are made from Aluminium EN AW-6060.

FE-Model

The single lap joint test specimens consist of two slotted aluminium flanges in which a thin CFRP laminate is glued with high conductive glue (ECCOBOND 285). The other laminates' ends are single lap jointed with a structural adhesive (Araldite 2014-1) as depicted in Fig. 6 and the corresponding parametric and simplified 3D FE model (Fig. 3). The latter one comprises entirely of HEX8 elements with a fixed base length and width of 1mm in the xy-plane, which is found after a convergence study to be the most suitable cell size for the following investigations. The z-directional element dimension can take theoretically any value. Each laminate (laminates-1 and

Tab. 2. Material conductivities.

Material	κ_A	κ_T
Aluminium EN AW-6060	205 W/mK (average) [17]	
Araldite 2014-1	0.23 W/mK*	
Scheuffler L160/H163	0.19 W/mK*	
ECCOBOND 285 (Catalyst 23 LV)	1.44 W/mK [18]	
M40J fibre	68.62 W/mK [19]	-
MTM46 neat resin	0.20W/mK (assumption)	
M40J-UD/MTM46, $f_{vol}=54\%$	37.15 W/mK (Eq. 2)	0.66 W/mK*

* THB measurement at DLR.

laminates) as well as the structural adhesive in the jointed area is simulated by two finite element layers in z-direction (see Fig. 3). Both their geometry and material properties are directly controlled by 13 independent parameters, while the flanges and the high conductive glue layers adapt the geometry according to the parametrical changes and thus maintain the boundary conditions. The 13 parameters, delineated in Fig. 3 and Fig. 4, are further classified in 7 geometric dimensions ($W, L_f, L_j, L_t, t_{lam1}, t_{lam2}, t_{glue-j}$) and 6 material properties ($\kappa_{glue-j}, \kappa_{lam1-11}, \kappa_{lam1-22}, \kappa_{lam2-11}, \kappa_{lam2-22}, \kappa_{lam2-33}$). From

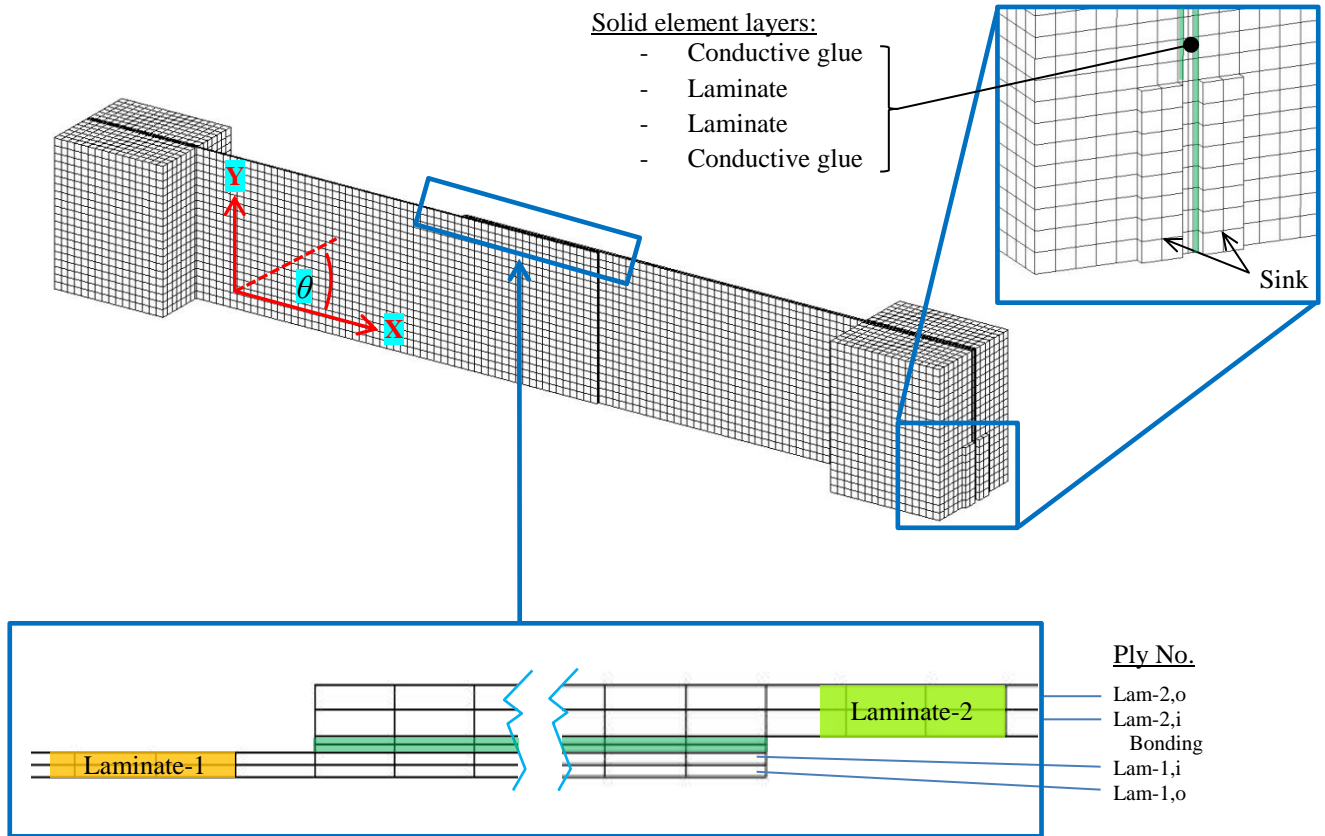


Fig. 3. Parametric 3D Finite Element Model of the test specimen and detail of the jointed and sink area.

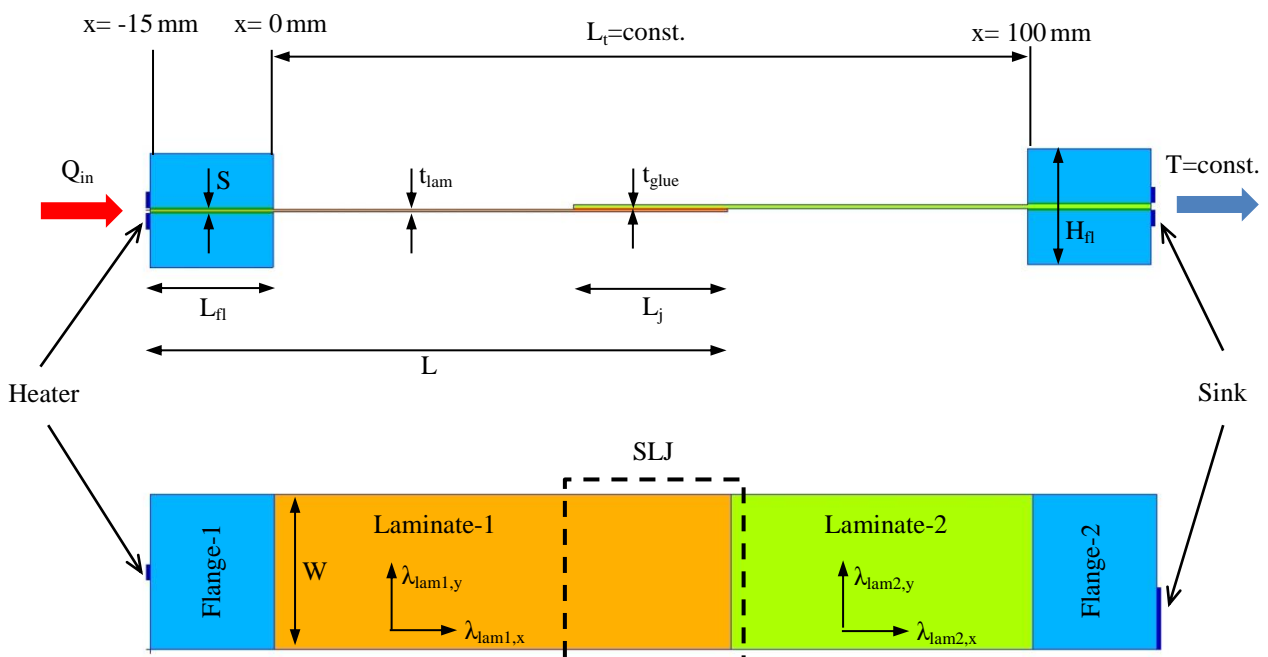


Fig. 4. FE model boundary conditions and model parameters.

these, the laminate's total length L_t and the flange's length L_{fl} are determined in a parameter study (cf. paragraph **Flange and total laminate's length sizing**). The properties of the aluminium flanges and the high conductive glue, which is simulated by a separate layer of HEX8 elements, are fixed. For simplicity the flanges are not fully modelled, but cut right at the end of the slit with a simulated opening $S \equiv t_{lam} + 2 * t_{glue-j}$ (see also Fig. 6, top right). The resistance heater and the sink are modelled by two halves that connect to the aluminium, as shown in the detail of Fig. 3. In total a heat load of 0.025 W is applied to the heater-related elements at flange-1 while the sink-related elements at flange-2 are constrained with a constant temperature of 298.15 K. Every contact in the model is assumed to be perfect and no additional resistances are implemented. Further no convection and radiation exchange is implemented.

Next to the 13 parameters which are considered in the sensitivity analysis there are a few more geometries and properties required for the model definition. All of them are depending on the controlled parameters such as the flanges width, for example, or they are set fixed. The fixed parameters are listed in Tab. 3.

Flange and total laminate's length sizing

The required flange's length L_{fl} and free laminate's length L (see Fig. 4) are investigated before the actual numerical analysis in a small parameter study and then set constant in the following. The reason for this parameter study is primarily that at the position $x=5$ mm and $x=95$ mm, where two of the temperature sensors are applied a quasi-1D temperature distribution must be guaranteed (cf. Fig. 8). For very thin laminates this shouldn't be a real issue. But considering a thicker laminate, as planned for future tests, a significant temperature gradient over the laminate's thickness can be reached. Further, ΔT has to be limited to ≈ 10 K due to the conductivity's temperature dependence.

As expected, the parameter study confirmed the assumption that the flange size's influence on the 1-D temperature profile can be neglected. The heat distributes very evenly and the temperature in the flange contact area is quasi-constant. Even a flange of $L_{fl}=5$ mm is still sufficient to guarantee a quasi-1D temperature profile, in in-plane and out-of-plane direction. Due to handling reasons $L_{fl}=15$ mm is selected and the total free laminate's length is set to $L_t=100$ mm.

3. ANALYTICAL CALCULATION

The analytical calculation is based on Fourier's law of heat conduction. In order to account for the different conductivities in the adherents and the jointed area, the test specimen is sub-divided in 5 consecutive sections as delineated in Fig. 5. According to the parameter study the laminates have a 1-D temperature distribution right after/before the clamping. Therefore the first section starts with the undisturbed laminate at $x=0$ mm and ends at $x=L-L_{fl}-L_j$. The second section is the jointed part of laminate-1 that is characterized by a heat flux in x- and z-direction. Next, the adhesive is considered as a separate third section before laminate-2 continues. Section S4 is again a transition area with x- and z-fluxes before section S5 is assigned from $x=L-L_{fl}$ to $x=2(L-L_{fl})-L_j$.

To determine the heat flux \dot{Q} in section S1 and S5, the integral form of Fourier's Law can be applied in the x-direction:

$$\dot{Q} = -\kappa_{Lam\#-11} * A_x * \frac{\Delta T}{\Delta x} \quad \text{with } \# = 1,2 \quad (5)$$

Tab. 3. Fixed geometric and material parameters.

Fixed 'Parameter'	Variable	Variable value
Width flange	W_{fl}	= W
Height flange	H_{fl}	14.75 mm
Thickness adhesive layer (flange)	$t_{glue,fl}$	0.2 mm
TC flange	$\lambda_{Aluminium}$	205 W/mK (see Tab. 2)
TC adhesive (flange)	$\lambda_{glue,fl}$	1.44 W/mK (see Tab. 2)

Rearranging Eq. 5 allows the definition of the heat flux density \dot{q} in x-direction:

$$\dot{q} = \frac{\dot{Q}}{A_x} = -\kappa_{lam\#-11} * \frac{\Delta T}{\Delta x} \quad \text{with } \# = 1,2 \quad (6)$$

Introducing the thermal resistance R_t in Eq. 6, it can be written as:

$$\dot{Q} = \frac{\Delta T}{R_t} \quad (7)$$

with

$$R_t = \frac{\Delta x}{A_x * \kappa} \quad (8)$$

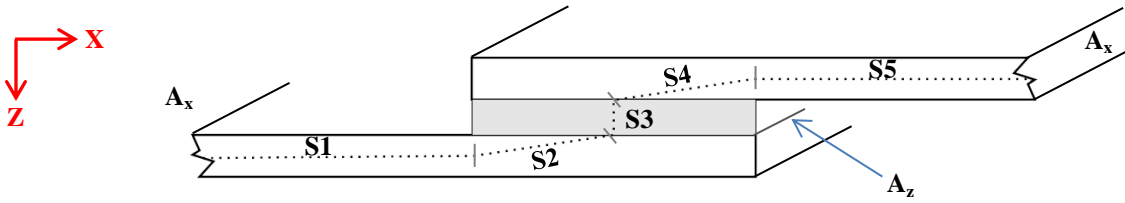


Fig. 5. SLJ sub-division with line of the ‘concentrated’ heat flux (dashed line).

For sections S2 to S4 the x-directional heat flux is superimposed by a z-directional one. Assuming an averaged heat flux as delineated in Fig. 5, a stepwise linear temperature decrease through the laminate’s thickness can be calculated. The heat flux passes first the half of the jointed area in laminate-1 in xz-direction (S2), then half of the adhesive layer’s cross section A_z in z-direction (S3) and again one half of the jointed area of laminate-2 in xz-direction (S4). Hence for section S2 and S4 Eq. 9 can be applied, averaging the fluxes in both directions.

$$R_t = \frac{\Delta x/2}{A_x * \kappa_{11}} + \frac{\Delta z/2}{A_z * \kappa_{33}} \quad (9)$$

In section S3 Eq. 8 shall be applied, yet in z-direction.

Mechanically, the SLJ is characterised by the shear tension peaks at both ends of the joint [20]. These depend on the jointed length $l_{\ddot{u}}$, the adherends’ stiffness ratio $\Psi=f(E,t)$, the adhesive’s shear modulus G_K and the adhesive layer’s thickness $t_{glue}=t_k$:

$$\frac{\tau_{K \max}}{\bar{\tau}_K} = \frac{\rho}{(1 + \Psi)} = \frac{l_{\ddot{u}}}{(1 + \Psi)} \sqrt{\frac{G_K(1 + \Psi)}{Et * t_K}} \quad (10)$$

The mean shear tension in the joint, introduced by a force F in x-direction is:

$$\bar{\tau}_K = \frac{F}{l_{\ddot{u}} * b} \quad (11)$$

Hence, relevant not only for the mechanical design is primarily the width of the joint $b = W$, which has an antiproportional influence on the height of the shear tension peaks $\tau_{K \max}$. The adherends’ and adhesive’s thickness t and t_k respectively, influence the joint’s shear strength only underproportional as $\tau_{K \max} \propto \sqrt{1/t * t_K}$. Thus both parameters are recommended to be included in the

thermal considerations only. For a mechanical evaluation, the results may be normalized to the width of the SLJ.

4. EXPERIMENT

The experimental setup delineated in Fig. 7 is based on a study performed by Baturkin [12]. It consists of two aluminium flanges (heater interface, cooling interface) that clamp the single lap jointed laminates. At the heater interface a $\approx 100 \Omega$ resistance heater is clamped at the flange and with thermal paste in between. Via voltage control the power is set to 0.1 W, which delivers an adequate temperature drop of approx. 10 K over the total specimen. The cooling interface is connected to a copper plate which is kept at a constant temperate ($T_{sink} = 298.15 \text{ K}$) by a liquid (nitrogen) thermostat. In order to generate the required power a constant voltage of $\approx 3.1 \text{ V}$ each is applied to the resistance heaters. The exact values depend on the actual contact resistances, radiation leaks etc. and are listed in Tab. 6. Both, the interfaces and the specimen are wrapped with a single layer insulation foil (SLI) and the covered by another 8 layers SLI (single layer insulation, coated Mylar® foil). This is fixed to the copper plate, which is covered with Mylar foil, too. The shroud of the thermal vacuum chamber has $(+22\dots25) \text{ }^\circ\text{C}$ and the vacuum in the chamber is kept at $1.5 \times 10^{-5} \text{ mbar}$ during the test. A detailed positioning of the TS is delineated in Fig. 8. At $x=-15 \text{ mm}$ and $x=100 \text{ mm}$ two control sensors are placed on the aluminium flanges.

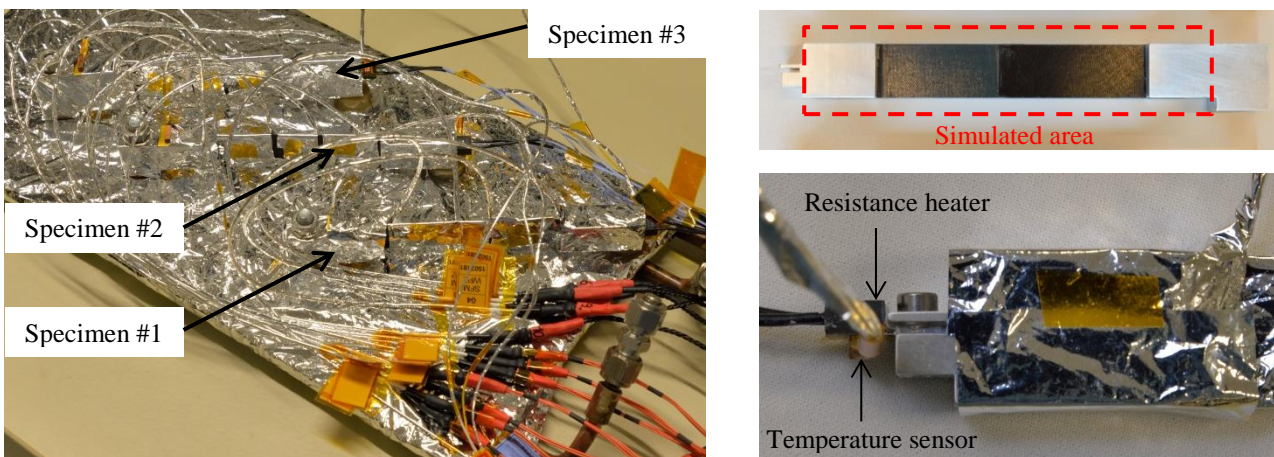


Fig. 6. Test setup with 3 specimen on the cold plate without the 8 SLI layers (left). Specimen #2 with highlight of the simulated area (top right) and resistance heater interface with temperature sensor (bottom right).

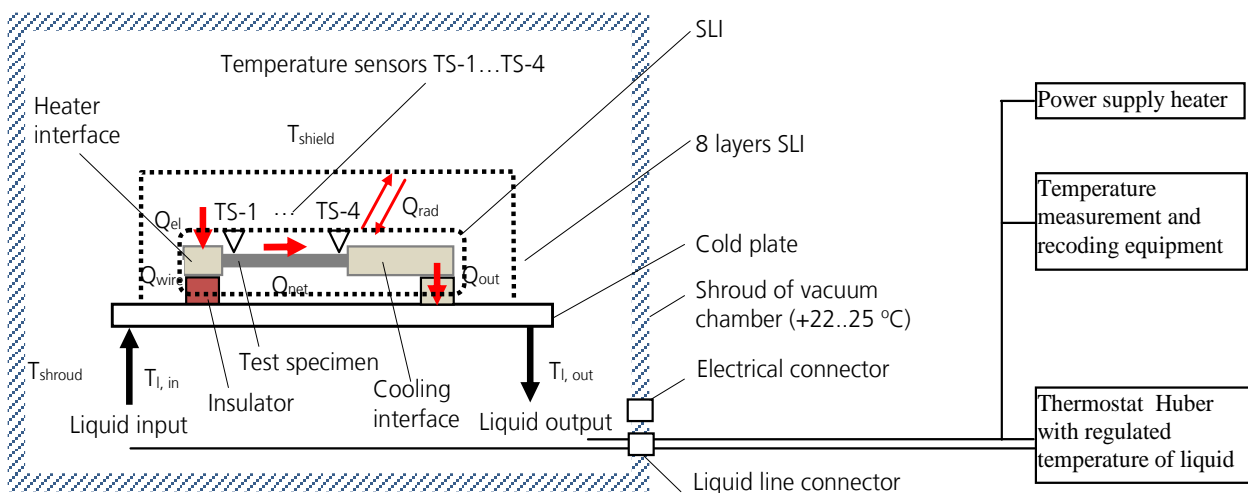


Fig. 7. Modified test setup for SLF conductivity measurements in TVAC chamber (sketch after [12]).

5. RESULTS

In the following the results obtained with the analytical and numerical calculation as well the experimental measurements are compared. An overview of all temperature sensor positions and additional evaluation points is delineated in Fig. 8. In bold letters the four temperature sensors (TS) that are evaluated in every measurement and calculation, though for case #2 the absolute position of TS-2 and TS-3 differs due to the extended joint area L_j . Sensor TS-0 as well as the other positions are only ‘virtual’ for the comparison of the analytical and numerical results. Both evaluate the TS-1 to TS-4 in the middle of the laminates at $0.5 * t_{lam}$.

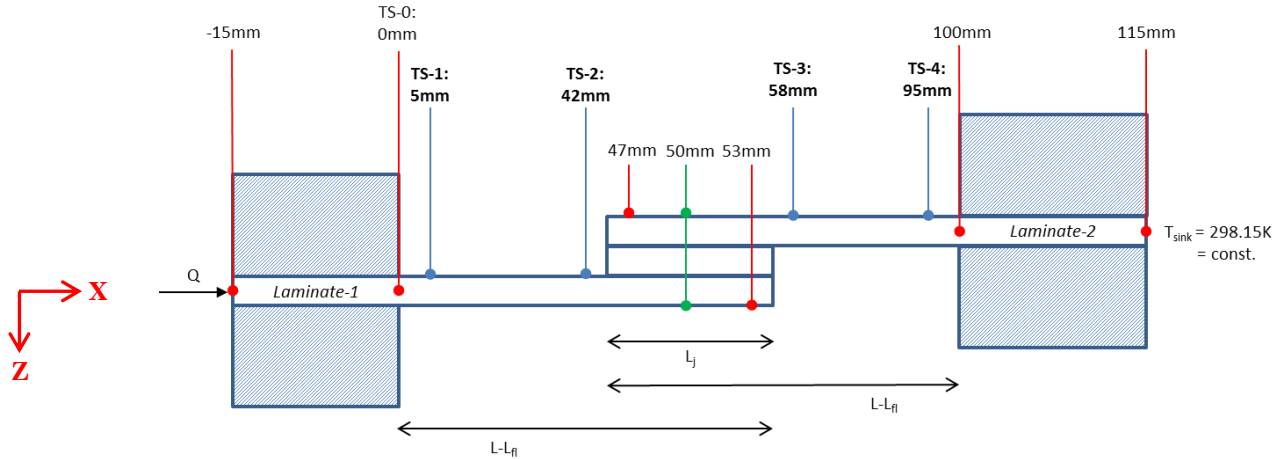


Fig. 8. Evaluated data points (case #1). Sensor position in y-direction: $y=W/2$.

Analytical Solution

Setting the heat flux $\dot{Q}=0.025$ W and applying eqs. 7 – 9 allows the calculation of the specimen temperature at every point with respect to the constant temperature at the sink $T_{sink} = 298.15$ K. Tab. 4 lists the calculated temperatures at the four TS positions, in the jointed area L_j and the temperature difference between sensor TS-1 and TS-4 ($\Delta TS-1/4$). As expected the thermal resistance and temperature differences respectively, change linear with the geometry. Case #3 shows a temperature drop of exactly $\Delta TS-1/4_{Case_#1} * 1.5 = \Delta TS-1/4_{Case_#3}$, which correlates with its 50% wider laminate compared to case #1. The local temperature drop over the SLJ, $\Delta TS-2/3$, is for case #1 and #3 approx. 18.0% of the total specimen’s temperature drop $\Delta TS-1/4$. For case #2 this ratio is approx. 27.5%, which is by a factor of 1.5 higher. Fig. 9 shows a graphical representation of the analytical results. Comparing the curves of case #1 and #2 they develop slightly different between TS-1 and TS-4, although the temperature difference $\Delta TS-1/4$ is the same. The reason is the differing sensor x-position, which is even more apparent for $\Delta TS-2/3$. Because of the same reason, a normalisation of $\Delta TS-2/3$ to the corresponding joints’ lengths results in 0.17 K/mm for case #1 and 0.13 K/mm for case #2. For case #3 the normalized temperature drop is $\Delta TS-2/3=0.11$ K/mm.

Tab. 4. Analytical results in degrees Kelvin for $x=0...100$ mm.

Test Case	TS-0 $x=0$	TS-1 $x=5$	TS-2 $x=42$ $x=37(\#2)$	$x=47$	$x=50_{lam2}$ $x=50_{am1}$	$x=53$	TS-3 $x=58$ $x=63(\#2)$	TS-4 $x=95$	T_{sink} $x=100$	$\Delta TS-1/4$	$\Delta TS-2/3$
#1	308.67	307.99	302.94	301.84	301.72	301.57	301.20	298.45	298.15	9.54	1.74
#2	308.59	307.92	303.47	301.88	301.54	301.13	300.84	298.39	298.15	9.53	2.63
#3	305.16	304.71	301.34	300.61	300.53	300.43	300.18	298.35	298.15	6.36	1.16

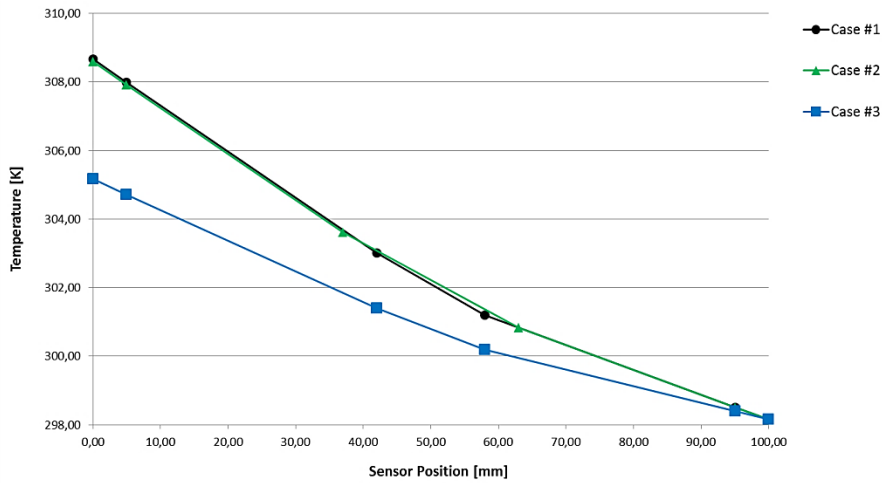


Fig. 9. Temperature gradients in the specimens. Analytical calculation.

Numerical Solution

In the following the results of the FE simulation are presented. Fig. 10 (top) shows for case #1 the temperature plot of the ‘undisturbed’ areas, id est $x=5\dots42$ mm and $x=58\dots95$ mm. As in the analytical calculation, these areas are characterized by a continuous 1-dimensional temperature gradient correlating with the different effective conductivities in laminate-1 and laminate-2. In contrast, the close-up of the SLJ in ‘side view’ shows quiet steep and 2-dimensional temperature gradients in the joint’s transition areas. Fig. 11 and Fig. 12 show the heat flux density distributions in the SLJ. Fig. 12 indicates that the highest heat flux occurs at the edge $x=L-L_{fl}-L_{j1}$ and slightly lower, but still high, at $x=L-L_{fl}$. At the edge $x=L-L_{fl}-L_{j1}$ it concentrates mostly in the adhesive layer and in the inner half of laminate-2, id est Lam-2,i (cf. Fig. 3). At the other end the highest heat flux is mostly present in the adhesive layer. Especially the z-directional flux component (cf. Fig. 12) is present in the first and last $\approx 20\%$ of the SLJ’s length. Its rate is there about two times higher than in the centre. This leads to prompt and local temperature compensations between the two adherends as described before for Fig. 10. Hence, the temperature in through-the-thickness direction is quasi-constant at the half length of the SLJ ($x=50$ mm). Fig. 13 shows the z-directional heat flux density for case #2. The jointed length $L_{j2}=2*L_{j1}$ has compared to case #1 an intermediate zone with almost

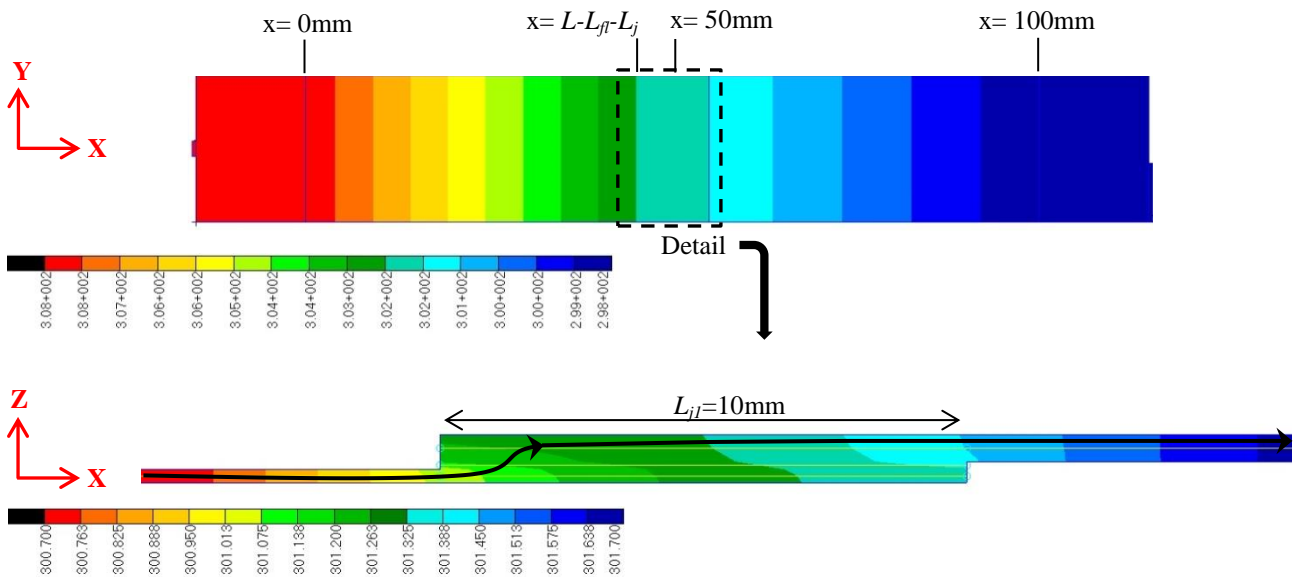


Fig. 10. Temperature plot, Case #1. Overview (top) and detailed ‘side view’ of the jointed area with a schematic heat flux stream line (bottom).

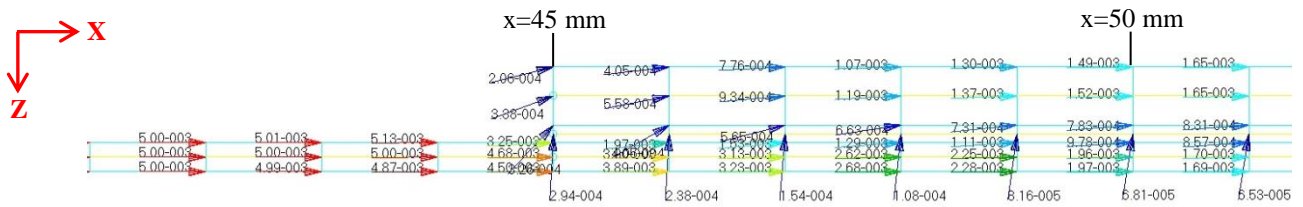


Fig. 11. Heat flux density vector field (magnitude), case #1 (detail view of jointed area).

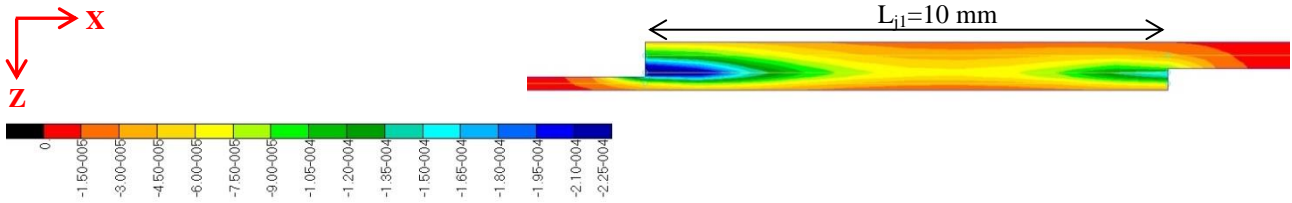


Fig. 12. Heat flux density plot in z-direction, case #1 (detail view of jointed area).

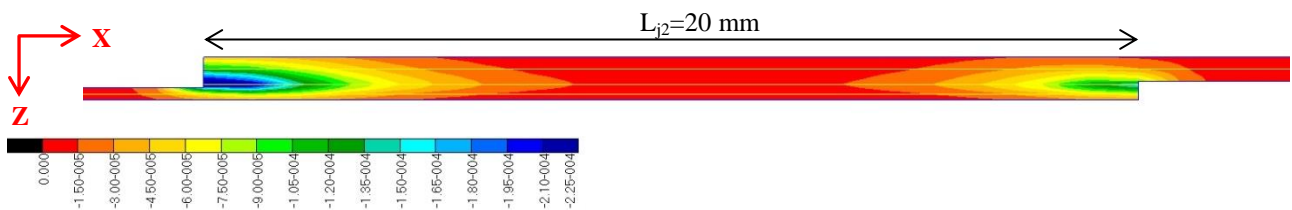


Fig. 13. Heat flux density plot in z-direction, case #2 (detail view of jointed area).

Zero z-directional heat flux density. The length of this zone extends about 30% of the total jointed length and completely through-the-thickness. At the edge $x=L-L_{fl}-L_{j1}$ the heat flux vector field is qualitatively and quantitatively the same as for case #1 and #2. Case #3 shows qualitatively the same temperature and heat flux distribution as case #1. Quantitatively the temperature differences are 50% lower than for case #1, which results from the 50% lower thermal resistance.

Next to the preceding graphical representations, Tab. 5 shows an extract of the numerically calculated temperatures. Comparing the temperature values indicates that for each case at $x=50$ mm a quasi-constant temperature in the joint's cross section is reached. The total temperature difference $\Delta TS-1/4$, however, is for case #1 higher than for case #2, which signifies a slightly higher effective conductivity of the longer SLJ in case #2. Focussing on $\Delta TS-2/3$ requires again a normalisation with the SLJ's length and results for case #1 in a temperature drop of $\Delta TS-2/3_{norm} = 0.14$ K/mm. In contrast, case #2 and #3 have an almost identical behaviour with a smaller normalized temperature drop of $\Delta TS-2/3_{norm} = 0.09$ K/mm. Fig. 14 reveals the differences in the analytically and numerically calculated temperatures from Tab. 4 and Tab. 5 respectively. Qualitatively the curves have the same trend. While the deviations in the area $x=42\dots 100$ mm are smaller, they are approximately two times higher in the area $x=0\dots 41$ mm. Furthermore for case #1 and #3 the differences are smaller than for case #2. The experimental results contained in Fig. 14 are presented in the next paragraph.

Tab. 5. Numerical results in degrees Kelvin for $x=0\dots 100$ mm.

Test Case	TS-0 $x=0$	TS-1 $x=5$	TS-2 $x=42$ $x=37(\#2)$	$x=47$ $x=42(\#2)$	$x=50_{lam2}$ $x=50_{lam1}$	$x=53$ $x=58(\#2)$	TS-3 $x=58$ $x=63(\#2)$	TS-4 $x=95$	T_{sink} $x=100$	$\Delta TS-1/4$	$\Delta TS-2/3$
#1	308.33	307.67	302.69	301.90	301.80 301.89	301.76	301.32	298.63	298.15	9.04	1.37
#2	307.76	307.10	302.79	302.01	301.70 301.71	301.38	300.95	298.63	298.15	8.47	1.84
#3	304.96	304.52	301.20	300.68	300.61 300.67	300.58	300.29	298.50	298.15	6.02	0.91

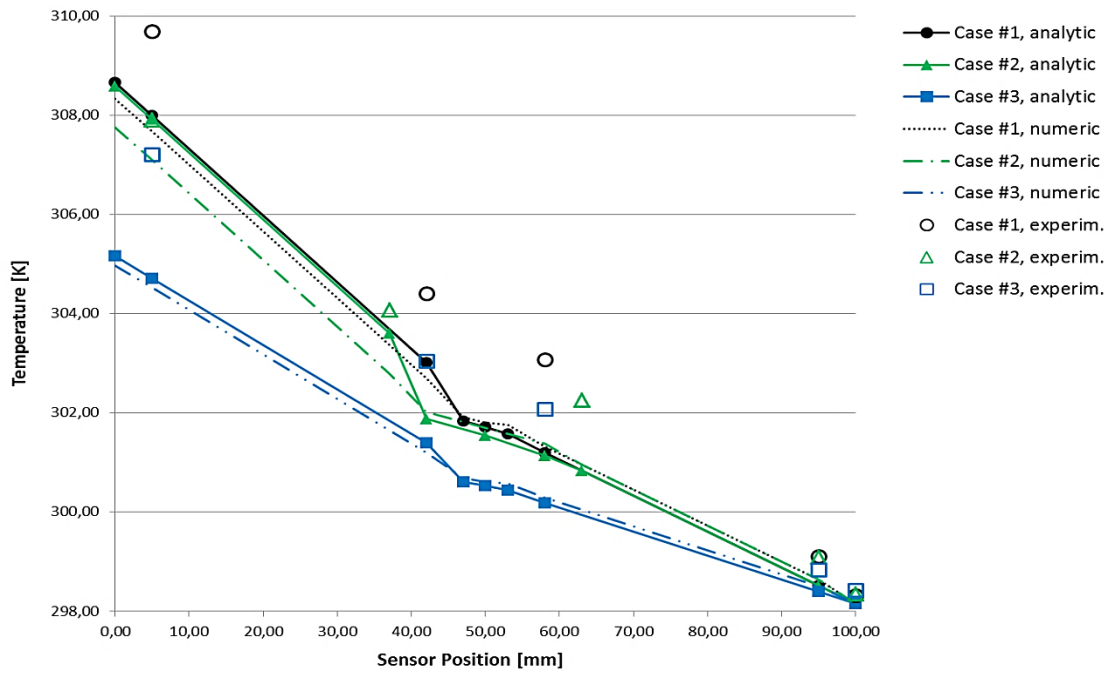


Fig. 14. Comparison of analytical and numerical temperature calculations incl. experimental results.

Experimental Results

Tab. 6 contains the measured steady-state (ΔT per hour = ± 0.1 K) results. The thermostat was set to $T_{l,in} = 24.7 \pm 0.1$ °C and the temperature at the cooling interfaces reached in average 25.22 °C. TS-4, the first temperature sensor next to the cooling interface (cf. Fig. 8) reached for case #1, #2 and #3 a steady-state temperature of 29.95 °C, 29.94 °C and 29.68 °C respectively. This is between 0.4 K and 0.7 K higher than at the cooling interface. Comparing the absolute temperature values of the following sensors (TS-3 to TS-1) the differences between simulation and measurement increase with the distance from the cooling interface at $x = 100$ mm (cf. Fig. 14). An exception to this trend is the measurement at TS-1, case #2. The general trend is emphasized by Tab. 7, which shows the direct comparison of the numerical and experimental results. There is a very good agreement with the temperature drop $\Delta TS-2/3$, but on a wider range the agreement with $\Delta TS-1/4$ is rather poor. The absolute values for case #1 and #3 differ considerably from the simulation and also the relative difference between $\Delta TS-1/4_{Case_#1}$ and $\Delta TS-1/4_{Case_#3}$ is not matching the expected factor of 1.5.

Tab. 6. Experimental results for $x = -15 \dots 100$ mm. Temperatures in degrees Kelvin.

Test Case	\dot{Q} [W]	T_{heater}	TS-1 $x = 5^*$	TS-2 $x = 42^*$ $x = 37(\#2)^*$	TS-3 $x = 58^*$ $x = 63(\#2)^*$	TS-4 $x = 95^*$	T_{sink}	$\Delta TS-1/4$	$\Delta TS-2/3$
#1	0.10 ± 0.01	311.57 ± 0.1	309.69 ± 0.1	304.40 ± 0.1	303.08 ± 0.1	299.10 ± 0.1	298.31 ± 0.1	10.59 ± 0.2	1.32 ± 0.2
#2	0.10 ± 0.01	310.23 ± 0.1	307.91 ± 0.1	304.08 ± 0.1	302.26 ± 0.1	299.09 ± 0.1	298.35 ± 0.1	8.82 ± 0.2	1.82 ± 0.2
#3	0.10 ± 0.01	308.64 ± 0.1	307.21 ± 0.1	303.04 ± 0.1	302.07 ± 0.1	298.83 ± 0.1	298.43 ± 0.1	8.38 ± 0.2	0.97 ± 0.2

* ± 0.2 mm

Tab. 7. Comparison of numerical and experimental results. Temperatures in degrees Kelvin.

Test Case	Δ : numerical minus experimental results						
	TS-1	TS-2	TS-3	TS4	T_{sink}	$\Delta TS-1/4$	$\Delta TS-2/3$
#1	2.02 ± 0.1	1.71 ± 0.1	1.76 ± 0.1	0.47 ± 0.1	0.16 ± 0.1	1.59 ± 0.2	-0.04 ± 0.2
#2	0.81 ± 0.1	1.29 ± 0.1	1.31 ± 0.1	0.46 ± 0.1	0.20 ± 0.1	0.38 ± 0.2	-0.01 ± 0.2
#3	2.69 ± 0.1	1.84 ± 0.1	1.78 ± 0.1	0.33 ± 0.1	0.28 ± 0.1	2.79 ± 0.2	0.10 ± 0.2

6. CONCLUSION

The paper compared analytically, numerically and experimentally the temperature distribution in 3 SLJ specimens under high vacuum conditions (1.5×10^{-5} bar) at 25 °C. It is found that for two cases (#1 and #3) the analytical and numerical results agree quite well along the entire specimen. In laminate-1, however, the deviations are higher than in laminate-2. For case #2 the numerical results deviate from the analytical ones in the area $x=0 \dots 41$ mm (Tab. 4 and 5). In general, the numerical results cannot confirm the assumption, which is made in the analytical solution for the description of the temperature gradient in jointed area itself (Eq. 8). The temperature decrease in the sections S2 and S4 does not extend over the half length of each laminate's jointed area. Hence, it is proposed to further investigate two approaches for a better semi-analytical description of the heat flux and temperature distribution within the SLJ, respectively:

- *Shear load analogy:*
The heat flux peaks in the transition areas of the SLJs might be described with an approach as used for the shear stresses occurring in the adhesive layer. Therefore in Eq. 2 the components describing the stiffness could to be exchanged by conductivities.
- *Virtual convection zone:*
For rather 'long' joints the heat flux distribution might be approximated by a virtual convection zone between the adhesive layer and laminate-2.

The experimental investigation shows very good results for the prediction of the temperature gradient $\Delta T_{S-2/3}$. $\Delta T_{S-1/4}$, however, does not match well with the analytical and numerical results. A reason might be found at the heater interface, where the measured temperature differences between T_{heater} and TS-1 scatter noticeably (1.43 – 2.32 K). This leaves room for uncertainties in the thermal contact resistances, occurring between the resistance heater and the flange as well as between the flange and the sample. Secondly, the temperature drop on laminate-1 ($\Delta T_{S-1/2}$) and laminate-2 ($\Delta T_{S-3/4}$), respectively, should be for each case similar, as the separate laminate's conductivity does not change from case to case. Though, the normalized temperature drops differ up to 25%, which might result from deviations in the fiber angles/ply orientation, contact resistances between sensor and specimen (cf. 'outlier' at TS-1, case #2), radiation effects etc. These open questions require further detailed investigations, which are at point of publication not finished yet.

Hence, it is proposed to continue the validation and later results correlation with the following steps:

- Ultrasound investigation of the adhesive layer between specimen and flanges.
- Measure deviations of fibre angles in the specimen.
- Heat leaks through the wires and radiation effects.

Additionally also the following investigations are planned:

- Temperature measurement at $x=50$ mm and at both sides of the SLJ in order to verify whether the temperature is (as predicted by the simulations) constant through-the-thickness. Therefore another specimen with a slightly thicker joint, id est thicker laminates, has to be manufactured.
- Amending the test cases by considering also different layups and thicknesses of laminate-2. This will help to validate the semi-analytical description of the temperature distribution within the SLJ.

Only when the coupon tests and analyses are finalised, the next step can be the 'design-dependent translation' of the joints' or interfaces' properties into a 2D/3D FE model.

REFERENCES

- [1] Mitsubishi Chemical America, K13C2U - Coal tar pitch-based carbon fibers.
- [2] M. Klebor, O. Reichmann, E.K. Pfeiffer, A. Ihle, S. Linke, C. Tschepe, S. Röddecke, I. Richter, M. Berrill, J. Santiago-Prowald, Latest progress in novel high conductivity and highly stable composite structure developments for satellite applications, in: ESA Communications (Ed.), Proc. of 12th European Conference on Spacecraft Structures, Materials & Environmental Testing, 2012.
- [3] A. Ihle, D. Hartmann, T. Würfl, O. Reichmann, V. Liedtke, C. Tschepe, M. Berill, High conductivity CFRP sandwich technologies for platforms, in: ESA Communications (Ed.), Proc. of 13th European Conference on Spacecraft Structures, Materials & Environmental Testing, 2014.
- [4] H. Katajisto, T. Brander, M. Wallin, Structural and Thermal Analysis of Carbon Composite Electronics Housing for a Satellite, in: Component and System Analysis Using Numerical Simulation Techniques - FEA, CFD, MBS, 2005.
- [5] M.R. Kulkarni, R.P. Brady, A model of global thermal conductivity in laminated carbon/carbon composites, *Composites Science and Technology* 57 (1997) 277–285.
- [6] J. Noack, Eine schichtweise Theorie und Numerik für Wärmeleitung in Hybridstrukturen, Shaker-Verlag, Aachen, 2000.
- [7] R. Rolfes, F. Ruiz-Valdepenas, M. Taeschner, R. Zimmermann, Fast Analysis Tools for Concurrent/Integrated Engineering of Composite Airframe Structures, in: International Conference on Optimization in Industry II, 1999.
- [8] L. Celotti, M. Solyga, R. Nadalini, V. Kravets, S. Khairnasov, V. Baturkin, C. Lange, R. Findlay, C. Ziach, T.-M. Ho, MASCOT thermal subsystem design challenges and solution for contrasting requirements, in: 45th International Conference on Environmental Systems, 2015.
- [9] D.G. Gilmore (Ed.), *Spacecraft Thermal Control Handbook: Volume I: Fundamental Technologies*, second ed., AIAA, Reston, Virginia (USA), 2002.
- [10] P. Kohnke, The implementation and integration of layered thermal shell element into a general purpose finite element program, in: Proceedings of NAFEMS World Congress 2003, NAFEMS, 2003.
- [11] M.W. Pilling, B. Yates, M.A. Black, The thermal conductivity of carbon fibre-reinforced composites, *Journal of Material Science* 14 (1979) 1326–1338.
- [12] V. Baturkin, Definition of longitudinal thermal conductivity of MESS element and Lander structure: Elaboration of the test procedure, estimation possible errors of measurements, RY-MTS HB, 2016.
- [13] M. Lange, C. Hühne, O. Mierheim, Detailed structural design and corresponding manufacturing techniques of the MASCOT Landing Module for the Hayabusa2 mission, in: Proceedings of 66th International Astronautical Congress, 2015.
- [14] L.N. McCartney, A. Kelly, Effective thermal and elastic properties of $[+\theta/-\theta]_s$ laminates, *Composites Science and Technology* 67 (2007) 646–661.
- [15] A. Pramila, Coupling term makes temperature fields unsymmetric in laminated composite plates, *Computers & Structures* 66 (1998) 509–512.
- [16] U. Hammerschmidt, V. Meier, New Transient Hot-Bridge Sensor to Measure Thermal Conductivity, Thermal Diffusivity, and Volumetric Specific Heat, *International Journal of Thermophysics* 27 (2006) 840–865.
- [17] Honsel AG, *Handbuch der Kentwerkstoffe (Handbook of Wrought Alloys)*.
- [18] Hysol, ECCOBAND 285: Thermally Conductive, Epoxy Paste Adhesive: (now sold as: Loctite Ablestik 285).
- [19] Toray Carbon Fibers America, M40J Data Sheet.
- [20] H. Schürmann, *Konstruieren mit Faser-Kunststoff-Verbunden*, Springer, Berlin Heidelberg, 2005.